Chapter 2
Nano-Cage Structured Materials: Clathrates

Toshiro Takabatake

Abstract Intermetallic clathrates are the representative of nano-cage structured material. A dimorphic clathrate $Ba_8Ga_{16}Sn_{30}$ possesses type-I and type-VIII structures. The type-I compound displays the glasslike thermal conductivity with a plateau at 4–12 K, which is ascribed to the strong interaction of acoustic phonons with the low-energy off-center rattling mode. In the type-VIII compound, the Ba guest is vibrating nearly on center of the distorted dodecahedron. Nevertheless, the thermal conductivity is as low as 0.7 W/Km for $T > 300$ K. The carrier type and its density in single crystals can be tuned by controlling the initial amount of flux, Ga or Sn. Further optimization of carrier density by alloying has led to high ZT of 1.0 and 1.45 for p- and n-type, respectively, at around 500 K, where the conventional materials based on Bi-Te and Pb-Te had a valley in ZT. By assembling p- and n-type legs made of $Ba_8Ga_{16}Sn_{30}$, a module was prepared with the segments of Bi-Te legs. The conversion efficiency reached 7.5 % at the temperature difference of 390 K.

2.1 Introduction

A basic concept "phonon-glass electron-crystal" (PGEC) for high performance thermoelectric materials was proposed by Slack in 1995 [1]. The PGEC materials are expected to have low thermal conductivity κ like a glass and simultaneously low electrical resistivity ρ like a metal. Such a material would achieve a high value of the dimensionless figure of merit defined as $ZT = \alpha^2 T/\rho\kappa$ if the Seebeck coefficient α is large enough. As a candidate, Slack mentioned compounds encapsulating guest atoms whose translational positions or angular orientations are not exactly defined. In such a system, the guest atom can move around the center in the cage. This off-center motion is expected to scatter the heat flow, and thus decreases the

T. Takabatake (✉)
Graduate School of Advanced Sciences of Matter and Institute for Advanced Materials Research, Hiroshima University, Higashi-Hiroshima 739-8530, Japan
e-mail: takaba@hiroshima-u.ac.jp

K. Koumoto and T. Mori (eds.), *Thermoelectric Nanomaterials*, Springer Series in Materials Science 182, DOI: 10.1007/978-3-642-37537-8_2,

thermal conductivity as in a glass. The electrons, on the other hand, can flow through the network of the cage as in a crystalline metal. According to this guiding principle, caged compounds such as filled skutterudites [2–5] and intermetallic clathrates [6–10] have been synthesized, and their physical and structural properties have been investigated extensively.

The term "clathrate" originates from the Latin *clathratus*, which means "protected by a cross bar." Intermetallic clathrates consist of three-dimensional frameworks of cages where guest atoms reside. Most of them are Zintl compounds in which the charge balance is well maintained between the guest ions and cage network. Therefore, stoichiometric clathrates show semiconducting behavior while small deviation from the ideal stoichiometry induces charge carriers in real samples. If the carrier density is tuned into the range $10^{19} - 10^{20}/\mathrm{cm}^3$, then high α (larger than $100\,\mu\mathrm{V/K}$) can coexist with low ρ of several mΩcm at room temperature [11, 12]. Low κ below $2\,\mathrm{W/Km}$ is also achieved in clathrates with a large mismatch between the guest ion size and the cage size [13, 14]. Thereby, the so-called *rattling*, large-amplitude anharmonic vibrations of the guest ion, scatters acoustic phonons carrying the heat. Furthermore, the anti-crossing of the acoustic mode with the guest vibration mode gives rise to the decrease of the group velocity of the acoustic mode. The rattling mode at low energy leads to increase of Umklapp scattering. These effects by rattling, anti-crossing, and Umklapp scattering suppress the lattice thermal conductivity although the detailed mechanism is still under debate [15–18].

This chapter describes the relationship between the structural and thermoelectric properties of intermetallic clathrates, especially, the dimorphic compound $Ba_8Ga_{16}Sn_{30}$ and related compounds.

2.2 Caged Structure of Intermetallic Clathrates

Intermetallic clathrates are classified into five types, I, II, III, VIII, and IX [8, 16, 19]. The structures of type-I, II, and VIII are displayed in Fig. 2.1. The general formula are described, respectively, as A_8E_{46}, $A_{24}E_{136}$, and A_8E_{46}, where A represents cationic guests and E represents cage atoms of group 14 elements Si, Ge, and Sn. The ternary

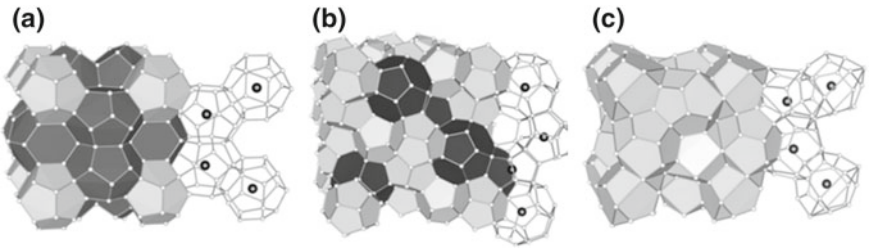

Fig. 2.1 Crystal structures of intermetallic clathrates of **a** type-I X_8E_{46}, **b** type-II $X_{24}E_{136}$, and **c** type-VIII X_8E_{46}. The unit cells of type-I, type-II, and type-VIII are composed of 2 dodecahedra and 6 tetrakaidecahedra, 16 dodecahedra and 8 hexakaidecahedra, and 8 distorted dodecahedra, respectively

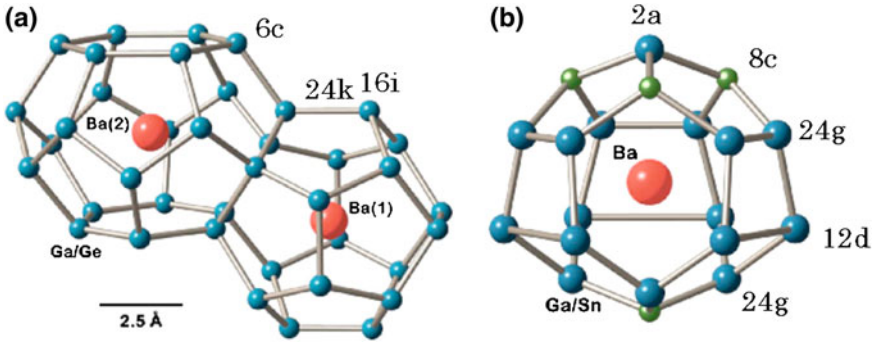

Fig. 2.2 Atomic configurations of cages and guests in **a** type-I and **b** type-VIII clathrates

derivative of type-I clathrate adopts the chemical formula $A_8E'_{16}E_{30}$, in which a group 13 element E′ is substituted for E. The guest atoms are encaged in tetrakaidecahedra and dodecahedra, as shown in Fig. 2.2. Among type-I clathrates, only four are known to have also type-VIII structure. They are $Ba_8Ga_{16}Sn_{30}$ [20, 21], $Eu_8Ga_{16}Ge_{30}$ [22], $Sr_8(Al,Ga)_{16}Si_{30}$ [23], and Sr_8 $(Al,Ga)_{16}Ge_{30}$ [24]. The dodecahedron in the type-I has high symmetry, whereas that in the type-VIII is distorted as shown in Fig. 2.2.

For most type-I clathrates, the guest in the tetrakaidecahedron occupies sites close to the 6*d* site at the cage center. Thereby, small off-centering occurs due to the disorder of cage atom occupations [16]. However, definite splitting of the guest site was revealed in type-I $Eu_8Ga_{16}Ge_{30}$ by neutron diffraction experiments [13]. The Eu atom moves off the 6*d* site about 0.4 Å to one of four equivalent positions 24 *k*, as shown in Fig. 2.3. Splitting with similar displacement was found in type-I $Ba_8Ga_{16}Sn_{30}$ by single crystal x-ray diffraction analysis [14]. It is worth noting that the off-center displacement increases as the temperature decreases. The isotropic displacement parameter for the Ba atom in the split site is still three times larger than that for the Ba atom in the dodecahedron. This splitting gives the guest atom freedom to move among the four sites, which gives rise to the strong interaction with the acoustic phonons as will be discussed later. On the other hand, the Ba atom in the dodecahedron in type-I $Ba_8Ga_{16}Sn_{30}$ was found to vibrate on center with the atomic displacement parameter similar as those of the cage atoms. In type-VIII $Ba_8Ga_{16}Sn_{30}$, however, the Ba atom in the distorted dodecahedron is vibrating on center with the atomic displacement parameter that is three times larger than those of cage atoms [25].

2.3 Band Structure and Electric Properties of $Ba_8Ga_{16}Sn_{30}$

Most intermetallic clathrates are Zintl compounds, in which the charge balance is well maintained between the guest ion and the cage network. In ternary clathrates $A_8E'_{16}E_{30}$, two electrons donated by each divalent A guest atom are accepted by

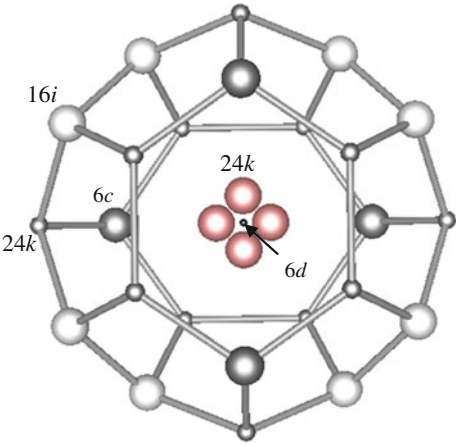

Fig. 2.3 Four split sites for the guest in the tetrakaidecahedron of type-I $Eu_8Ga_{16}Ge_{30}$ and $Ba_8Ga_{16}Sn_{30}$. The split sites 24*k* are 0.4 Å away from the cage center 6*d*

two E′ atoms of the group 13 element to form sp^3-like bonding. Accordingly, the electronic structure has a band gap at the Fermi level, which is approximately 0.5–0.9 eV for A = Sr, Ba, and Eu, E′ = Ga, and E = Ge [26]. The band calculations for type-I and type-VIII $Ba_8Ga_{16}Sn_{30}$ were performed by the full-potential linearized augmented plane wave method [27]. The results showed the presence of indirect gaps of 0.51 and 0.32 eV, respectively, as displayed in Fig. 2.4. For both types, the top of the valence bands consists of sp^3 bonding state of cage atoms Ga and Sn, while the bottom of the conduction bands consists of the anti-bonding state and the atomic orbitals of the Ba guest. Because the guests donate their electrons

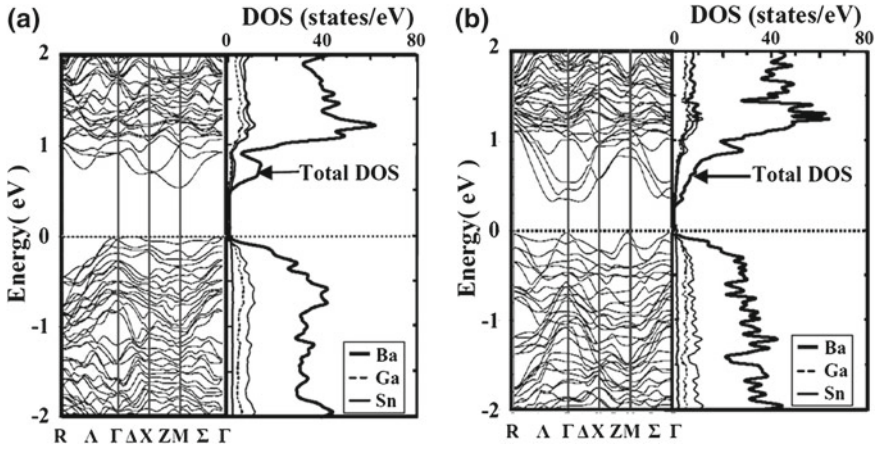

Fig. 2.4 Electronic band structure for **a** type-I and **b** type-VIII $Ba_8Ga_{16}Sn_{30}$

to anti-bonding states of the cage networks, the conduction bands are composed of orbitals of guest and cage atoms.

The steep slope in the density of states at the gap edges may give rise to a high Seebeck coefficient. In fact, the absolute values of $\alpha(T)$ at 300 K are 300 μV/K for both *p* and *n* type samples of the type-I $Ba_8Ga_{16}Sn_{30}$ [14], as shown in Fig. 2.5. The *p* and *n* type crystals were grown from Ga and Sn flux, respectively. The values of $\rho(T = 300\,\mathrm{K})$ are in the range 20–40 mΩcm, which is too large to be used as thermoelectric materials. This large resistivity is caused by the rather low carrier density of $10^{19}/\mathrm{cm}^3$ and rather low carrier mobility of 20–40 cm^2/Vs. Therefore, carrier doping by substitution of cage atoms should be effective to reduce the resistivity of type-I samples. As for the type-VIII samples, the thermoelectric data will be presented and discussed in Sect. 2.5.

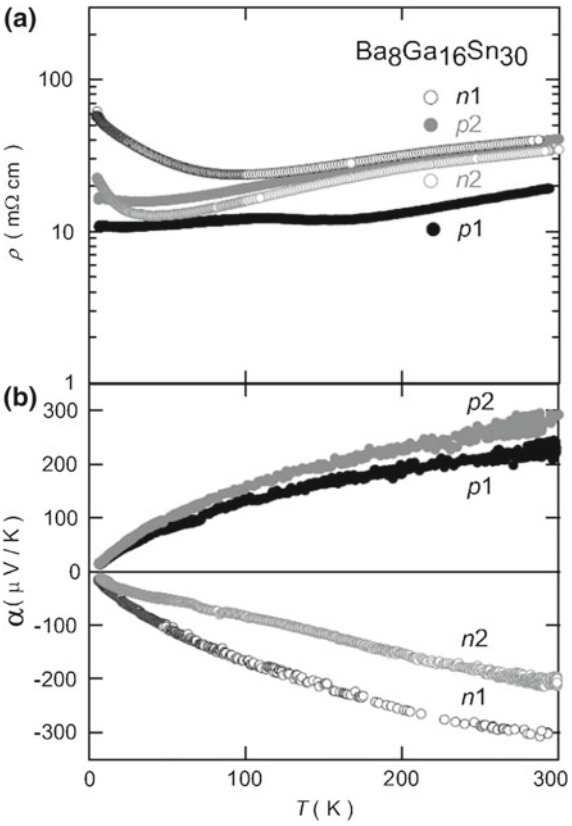

Fig. 2.5 Temperature dependence of **a** electrical resistivity ρ and **b** Seebeck coefficient α for type-I $Ba_8Ga_{16}Sn_{30}$ single crystals. The samples *p*1 and *p*2 are grown from Ga flux, while *n*1 and *n*2 are grown from Sn flux

2.4 Effect of Rattling on the Thermal Conductivity

Before discussing the "phonon-glass" behavior of intermetallic clathrates, it should be recalled what is the characteristic of the thermal conductivity of the glass. In Fig. 2.6b, the thermal conductivity of a typical glass, vitreous SiO_2, is displayed. It is characterized by T^2 dependence at low temperatures, a plateau at around 5 K, and roughly T-linear dependence above 10 K. The three characteristics are observed in the lattice thermal conductivity $\kappa_L(T)$ for type-I $Ba_8Ga_{16}Sn_{30}$, $Eu_8Ga_{16}Ge_{30}$, and $Sr_8Ga_{16}Ge_{30}$. Here, $\kappa_L(T)$ was obtained by subtracting the electric contribution $\kappa_e(T)$ from the measured thermal conductivity $\kappa(T)$. It is worth noting that the absolute value of $\kappa_L(T)$ of type-I $Ba_8Ga_{16}Sn_{30}$ at the plateau is still lower than that of vitreous SiO_2. By contrast, the $\kappa_L(T)$ for type-VIII $Ba_8Ga_{16}Sn_{30}$ with n-type carriers shows a peak at around 15 K, which is the behavior of a crystalline material [14, 28].

Let us discuss the relation between the phonon-glass behavior in $\kappa_L(T)$ and structural properties. For type-I $Ba_8Ga_{16}Sn_{30}$, $Eu_8Ga_{16}Ge_{30}$, and $Sr_8Ga_{16}Ge_{30}$, the guest atom in the tetrakaidecahedron occupies four split sites which are 0.3–0.4 Å away from the center as shown in Fig. 2.3. This splitting gives the guest atom freedom to

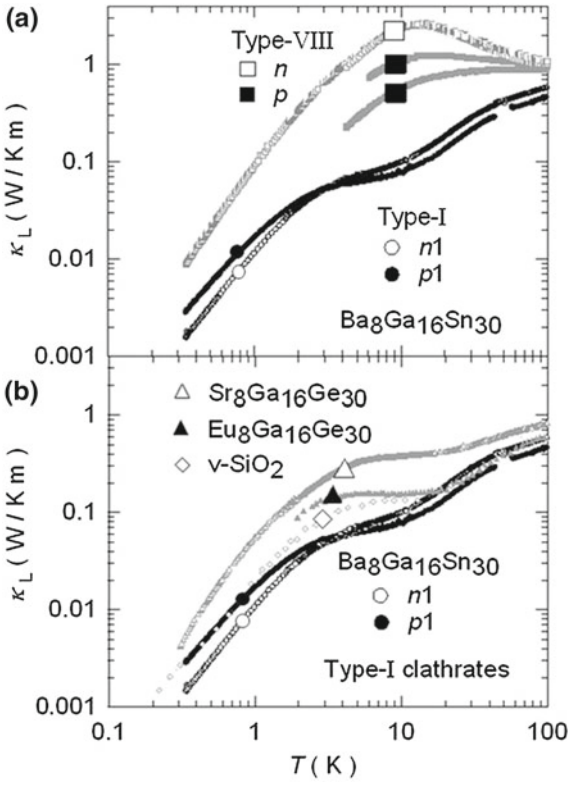

Fig. 2.6 Temperature dependence of lattice thermal conductivity κ_L for **a** type-I and type-VIII $Ba_8Ga_{16}Sn_{30}$, and **b** type-I $Ba_8Ga_{16}Sn_{30}$, $X_8Ga_{16}Ge_{30}$ (X = Sr, Eu), and vitreous SiO_2

move among the four sites. This "off-center rattling" may violate the translational symmetry and strongly interact with the acoustic phonons, which in turn reduces the thermal conductivity. This scenario was first proposed from the fact that the smaller guest ions lead to smaller $\kappa_L(T)$ among $A_8Ga_{16}Ge_{30}$ with A = Ba^{2+} (1.61 Å), Sr^{2+}(1.44 Å), and Eu^{2+} (1.35 Å) [13]. To examine this model, we plot in Fig. 2.7a the $\kappa_L(T)$ data at 150 K for various type-I clathrates reported so far against the cage radius [14]. The cage radius R_{cage} of the tetrakaidecahedron is defined as the distance from the 6*d* site at the center to the 24*k* site of the cage. The cage radius increases from 4.1 to 4.6 Å as the majority cage atom changes from Si, Ge to Sn, in the sequence of the increasing the covalent radius r_{cage} from 1.11, 1.22, to 1.41 Å. Among each series of compounds with Si, Ge, and Sn cages, κ_L decreases with the decrease of the guest ionic radius as illustrated by the guide lines in Fig. 2.7a. This relation in turn indicates that the relevant structural parameter is not the cage radius R_{cage} but the "free space" which is defined as $R_{free} = R_{cage} - r_{cage} - r_{guest}$, where $r_{guest}$is

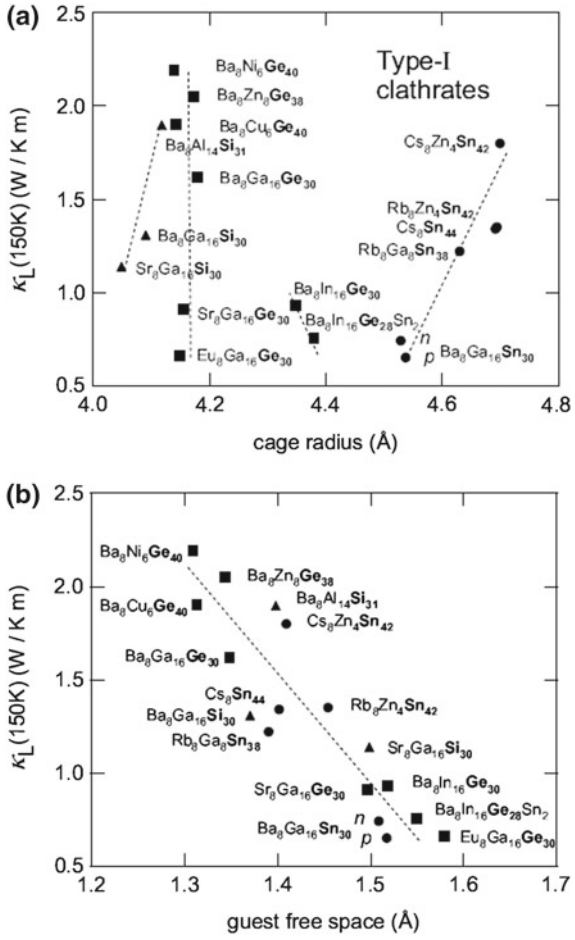

Fig. 2.7 Lattice thermal conductivity κ_L of various type-I clathrates at 150 K as a function of **a** cage diameter and **b** guest free apace

the ionic radius of the guest. In Fig. 2.7b, the data of $\kappa_L(T = 150\,K)$ are replotted against R_{free} [14]. We find that all data fall on a narrow band, indicating that the guest free space is the key parameter that determines the magnitude of κ_L for type-I clathrates. Among them, the lowest κ_L is realized in $Ba_8Ga_{16}Sn_{30}$ and $Eu_8Ga_{16}Ge_{30}$ with definite off-center rattling guests. This fact confirms that the off-center rattling effectively scatters the acoustic phonons to reduce the thermal conductivity at low temperatures.

2.5 Thermoelectric Properties of $Ba_8Ga_{16}Sn_{30}$ Above 300 K

In order to assess the ZT of the phonon-glass material $Ba_8Ga_{16}Sn_{30}$ for application thermoelectric generators, we measured the thermoelectric properties above room temperature. Figure 2.8 shows the $\kappa(T)$ of single crystalline samples of type-I and type-VIII [29]. The temperature range of the data for type-I is limited to 520 K because a structural transformation from type-I to type-VIII occurs at higher temperature [29, 30]. The $\kappa(T)$ for type-VIII is higher than that of the type-I, but the value of 0.7 W/Km is still comparable with that of the state-of-the-art materials based on Bi-Te and Pb-Te [11]. The upswing in $\kappa(T)$ for $T > 500\,K$ is attributed to the carrier excitations from the top of the valence band to the conduction bands, which is called the bipolar effect [31].

The data of $\alpha(T)$ and $\rho(T)$ for type-I $Ba_8Ga_{16}Sn_{30}$ with p- and n-type carriers are shown in Fig. 2.9. With increasing temperature, the absolute values of $\alpha(T)$ gradually increase to 460 μV/K at 520 K. The two curves of $\rho(T)$ also monotonically increase and are saturated at around 500 K. Using these data together with the $\kappa(T)$ in Fig. 2.8, $ZT = \alpha^2 T/\rho\kappa$ was estimated. The values are 0.37 at room temperature for both p- and n-types and have broad maxima of 0.58 and 0.50 at around 450 K, respectively [29].

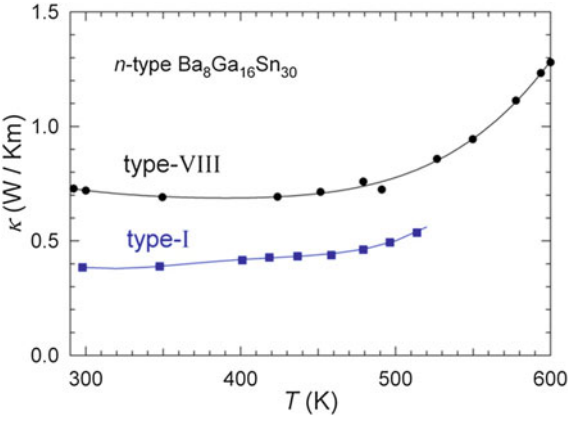

Fig. 2.8 Temperature dependence of thermal conductivity κ for the n-type samples $Ba_8Ga_{16}Sn_{30}$ with type-I and type-VIII structures

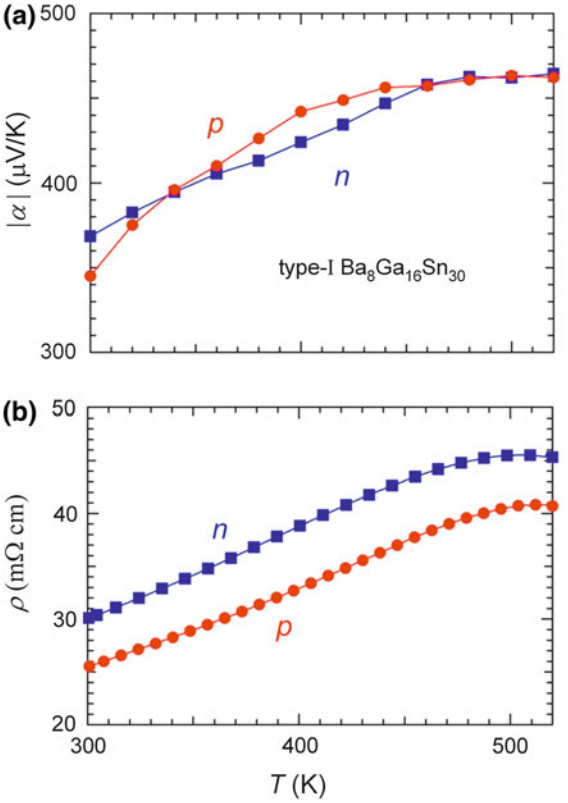

Fig. 2.9 Temperature dependences of **a** Seebeck coefficient and **b** electrical resistivity for the *p*- and *n*-type samples of type-I $Ba_8Ga_{16}Sn_{30}$

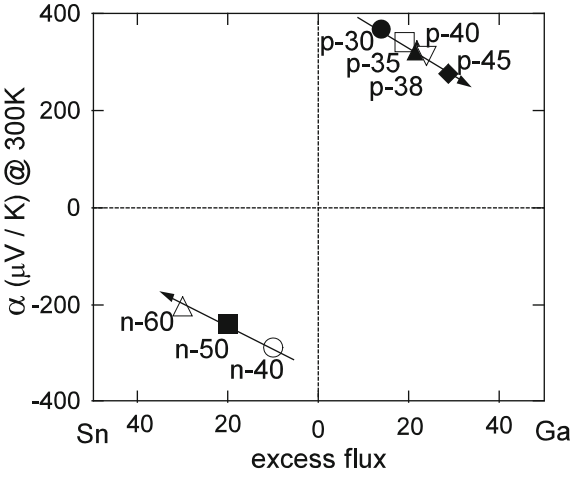

Fig. 2.10 Seebeck coefficient α at 300 K versus excess flux amounts for single crystals of type-VIII $Ba_8Ga_{16}Sn_{30}$. The data for crystals grown from Sn and Ga fluxes are shown in the left and the right, respectively

Now, we focus on type-VIII $Ba_8Ga_{16}Sn_{30}$ because it is more stable than the type-I at high temperatures. The carrier type can be tuned by the same method as for type-I. Actually, the growth of single crystals from Ga flux leads to *p*-type carriers and that from Sn flux leads to *n*-type carriers. Furthermore, we can tune the carrier density by controlling the excess flux amount. In fact, the value of $\alpha(T = 300\,\mathrm{K})$ systematically changes as a function of the excess flux amount, as shown in Fig. 2.10 [32]. On the right, α decreases linearly with increasing the excess amount of Ga from 14 (p-30) to 29 (p-45). The *p*-type carrier density gradually increases, while no significant change in the Ga composition of the crystal was observed. In the crystals grown from Sn flux, it was found that both the Sn composition and the *n*-type carrier density gradually increased as the excess amount was increased from 10 (n-40) to 30 (n-60) [32].

For carrier tuned *p*-type and *n*-type samples, temperature variations of α and ρ are displayed in Figs. 2.11 and 2.12, respectively. The $\alpha(T)$ of *p*-type samples exhibits a maximum whose temperature shifts toward higher side along with the decrease in the maximum value. The band gap E_g approximates twice the product of the maximum value and its temperature, $E_g = 2\alpha_{\max} \times T_{\max}$ [33]. The calculated value of 0.37 eV for E_g agrees with the value obtained by the band calculation [27]. The effect of

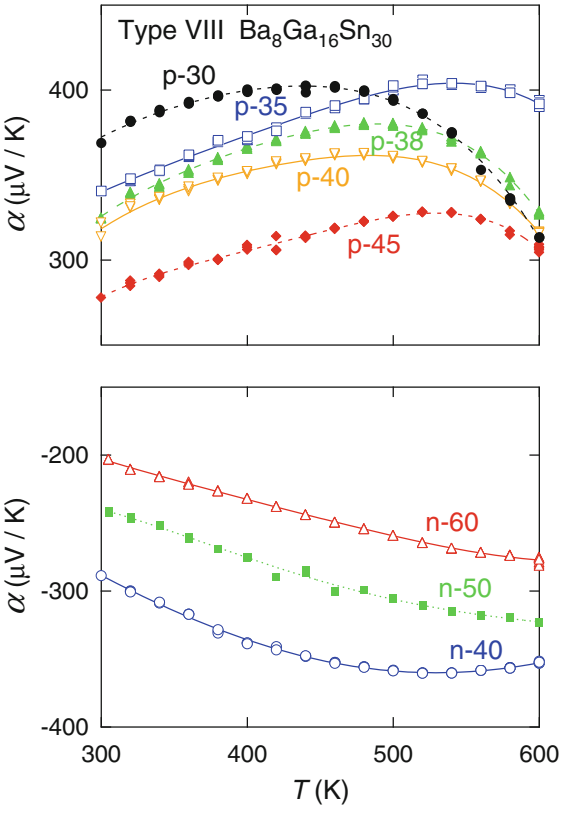

Fig. 2.11 Seebeck coefficient α as a function of temperature for type-VIII $Ba_8Ga_{16}Sn_{30}$ single crystals. The *p*-type samples and *n*-type samples were grown from Ga and Sn flux, respectively

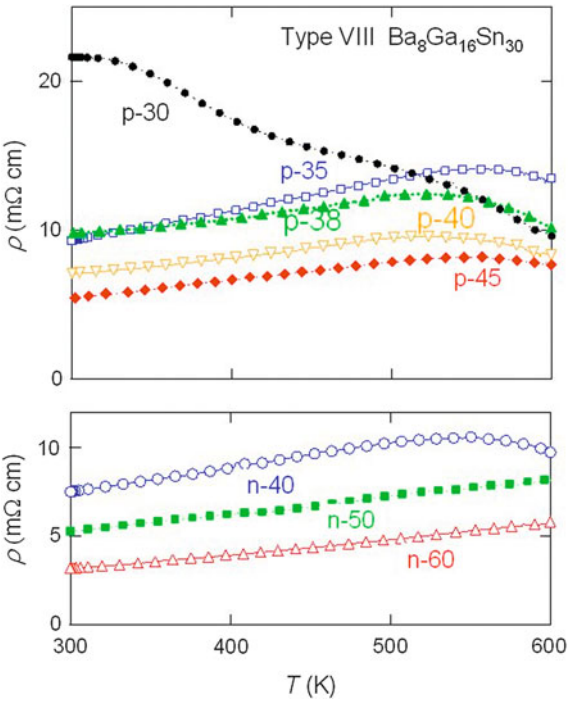

Fig. 2.12 Temperature dependence of electric resistivity ρ for type-VIII $Ba_8Ga_{16}Sn_{30}$ single crystals of *p*-type (*upper*) and *n*-type (*lower*)

carrier doping is manifested in the gradual decrease in the electrical resistivity to several mΩcm for both *p*- and *n*-types. In this sense, type-VIII $Ba_8Ga_{16}Sn_{30}$ can be transformed into an electron crystal by further doping of carriers, although it does not show phonon glass behavior at low temperatures. The *ZT* was evaluated by the use of the data of $\kappa(T)$ for the n-50 sample shown in Fig. 2.8. It was assumed that the bipolar contribution κ_b and the lattice part κ_L do not depend on the samples. Then, $\kappa(T)$ for each sample was calculated as $\kappa(T) = LT/\rho(T) + \kappa_L(\mathrm{n}-50) + \kappa_b(\mathrm{n}-50)$ with $L = 2.44 \times 10^{-8}\,\mathrm{W\Omega/K^2}$. The values of *ZT* are shown in Fig. 2.13. Among the *p*-type and *n*-type samples, p-40 and n-40 have the maximum *ZT* of 1.0 and 0.90 at round 450 K, respectively.

2.6 Substitution Effect on the Figure of Merit of Type-VIII $Ba_8Ga_{16}Sn_{30}$

In aiming at enhancing the *ZT* of type-VIII $Ba_8Ga_{16}Sn_{30}$, we made a systematic study by substituting various elements for the cage atoms Ga and Sn. We used isovalent elements Al and In for Ga [34], electron deficient elements Cu and Zn for Ga [35–37], isovalent Ge for Sn, and electron excess element Sb for Sn [32, 38]. Two examples, Al and Cu substitutions are described here. Because Ga is classified as a

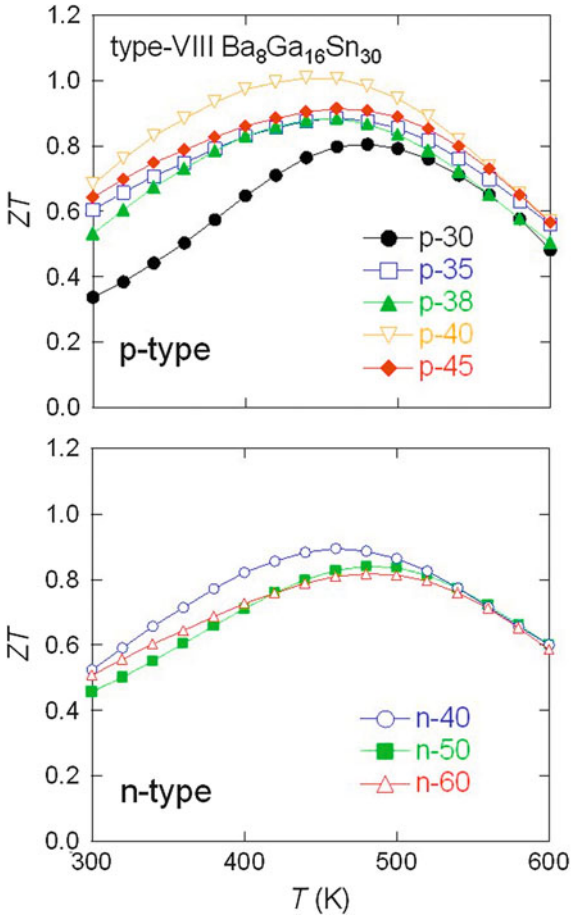

Fig. 2.13 Temperature dependence of the dimensionless figure of merit ZT for p-type (*upper*) and n-type (*lower*) samples of type-VIII $Ba_8Ga_{16}Sn_{30}$

rare element, the substitution of Al for Ga has the advantage of reducing the cost as well as lightening the weighs. The samples of $Ba_8Ga_{16-x}Al_xSn_{30}$ were prepared by the Sn flux method, thus the dominant carriers were n-type [34]. The lattice parameter increases linearly with increasing the Al content x up to the solubility limit of 10.5. The substitution with the isovalent Al may not change the carrier density. However, the electrical resistivity first decreases with increasing x up to 2, and then increases gradually for $x > 2$. A similar trend is found in the Seebeck coefficient. From $x = 0$ to $x = 2$, the absolute value of α decreases and then turns to increasing. The initial change in ρ and α with x up to 2 can be attributed to the increase in the carrier mobility. The thermal conductivity of all samples is almost the same up to 500 K. For $x = 6$, the upturn in $\kappa(T)$ due to the bipolar effect becomes weaker. As a result, the ZT for $x = 6$ is largely enhanced, and it reaches 1.2 at 500 K [34].

As a next step, we tried to dope holes in $Ba_8Ga_{16}Sn_{30}$ by substituting Cu which has two less electrons than Ga [35, 36]. However, the solubility of Cu was found to

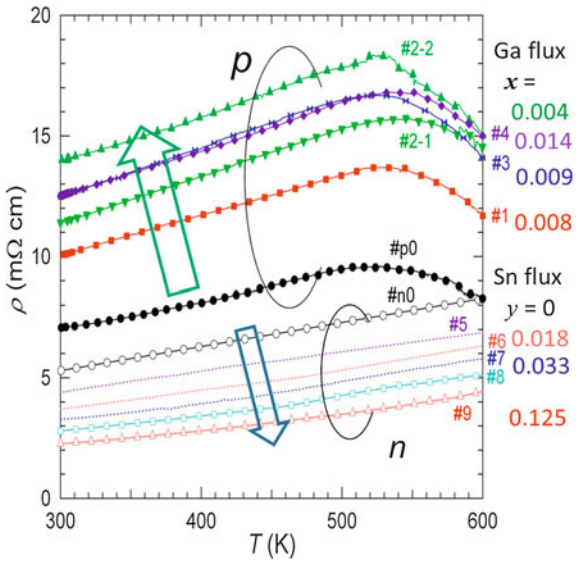

Fig. 2.14 Temperature dependence of electrical resistivity ρ for type-VIII $Ba_8Ga_{16}Sn_{30}$ doped with various amounts of Cu. $Ba_8Ga_{16-x}Cu_xSn_{30}$ single crystals of *p*-type were grown from Ga flux and $Ba_8Ga_{15.9-y}Cu_ySn_{30.1+y}$ single crystals of *n*-type were grown from Sn flux

be much lower than that of Al. In the crystals of $Ba_8Ga_{16-x}Cu_xSn_{30}$ grown from Ga flux, x is smaller than 0.014. For crystals grown from Sn flux, y is smaller than 0.125 in $Ba_8Ga_{15.9-y}Cu_ySn_{30.1+y}$, where the Sn composition is self-compensated. As is shown in Figs. 2.14 and 2.15, both the resistivity and Seebeck coefficient for *p*-type samples increase but no systematic trend with x or y is noticed due to the very low Cu content. The carrier density was found to be almost the same, meaning that we could not dope holes by Cu substitution. On the other hand, for the *n*-type samples, a more systematic change occurs in both the resistivity and Seebeck coefficient. The decrease in the resistivity is attributed to the doubling of the mobility because the carrier density is not changed. The data of $\kappa(T)$ are presented in Fig. 2.16. The value for the *p*-type sample is higher than the *n*-type samples although the reason is not clear yet. The bipolar effect on $\kappa(T)$ at $T > 500$ K is weakened in the *n*-type samples. By the Cu substitution, all the three quantities α, ρ, and κ, which are relevant in ZT, have decreased by different rates. As a result of the significant reduction in the resistivity by 50 %, the ZT of *n*-type samples is increased to 1.45 at 520 K, as in shown in (Fig. 2.17). This value is the highest among all substituted systems of type-VIII $Ba_8Ga_{16}Sn_{30}$.

2.7 Conclusion

We have described in this chapter how the concept of "phonon-glass electron-crystal" has guided the development of thermoelectric clathrates, especially $Ba_8Ga_{16}Sn_{30}$. The type-I $Ba_8Ga_{16}Sn_{30}$ has been proven to be a good example of phonon glass due to the strong interaction between the off-center rattling and acoustic phonons.

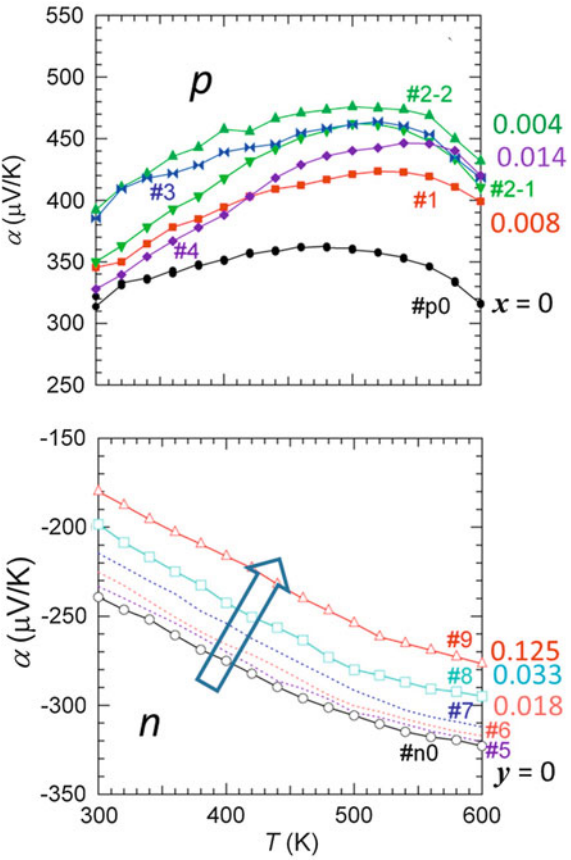

Fig. 2.15 Temperature dependence of Seebeck coefficient α for type-VIII $Ba_8Ga_{16}Sn_{30}$ doped with various amounts of Cu with compositions of $Ba_8Ga_{16-x}Cu_xSn_{30}$ and $Ba_8Ga_{15.9-y}Cu_ySn_{30.1+y}$

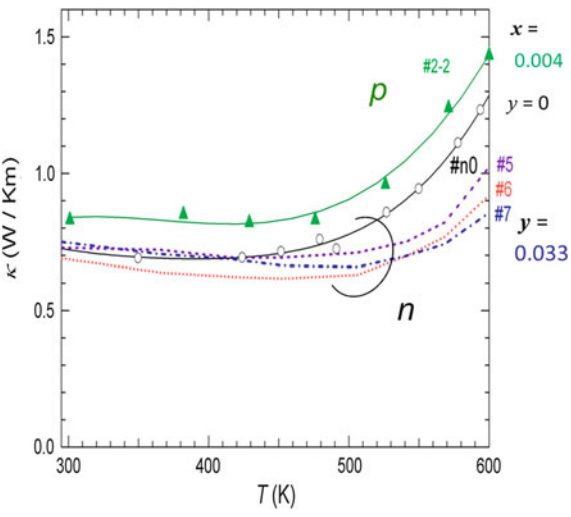

Fig. 2.16 Temperature dependence of thermal conductivity κ for type-VIII $Ba_8Ga_{16}Sn_{30}$ doped with various amounts of Cu with compositions of $Ba_8Ga_{16-x}Cu_xSn_{30}$ and $Ba_8Ga_{15.9-y}Cu_ySn_{30.1+y}$

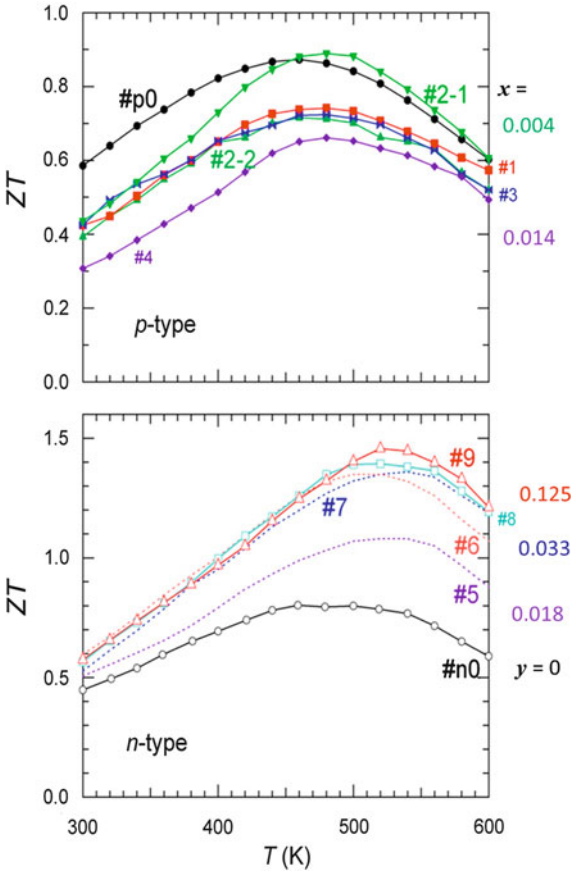

Fig. 2.17 Temperature dependence of *ZT* for type-VIII $Ba_8Ga_{16}Sn_{30}$ doped with various amounts of Cu with compositions of $Ba_8Ga_{16-x}Cu_xSn_{30}$ and $Ba_8Ga_{15.9-y}Cu_ySn_{30.1+y}$

The type-VIII $Ba_8Ga_{16}Sn_{30}$, on the other hand, shows better thermoelectric and structural properties above room temperature. As a summary, the *ZT* values of type-VIII $Ba_8Ga_{16}Sn_{30}$ and substituted samples are plotted based on the data reported for various thermoelectric materials [11]. As shown in Fig. 2.18, for both *p*-type and *n*-type materials, the valley in *ZT* at 200 °C has been the bottleneck for applications. Now, this valley is covered by the data for $Ba_8Ga_{16}Sn_{30}$ and substituted compounds. The $Ba_8Ga_{16}Sn_{30}$-based clathrate has the advantage that a module can be made from the same compound with both *p* and *n* types. This may prevent the module from degrading by thermal hysteresis. In fact, a module of 8 pairs of *p* and *n*-type elements was prepared, as shown in Fig. 2.19. When the Bi-Te legs were segmented to the legs made of $Ba_8Ga_{16}Sn_{30}$, the output power of 0.87 W was obtained at the temperature difference of 390 °C (Yamamoto, unpublished). This corresponds to a conversion efficiency of 7.5 %. Still higher efficiency should be obtained if the carrier densities in the $Ba_8Ga_{16}Sn_{30}$ legs are optimized.

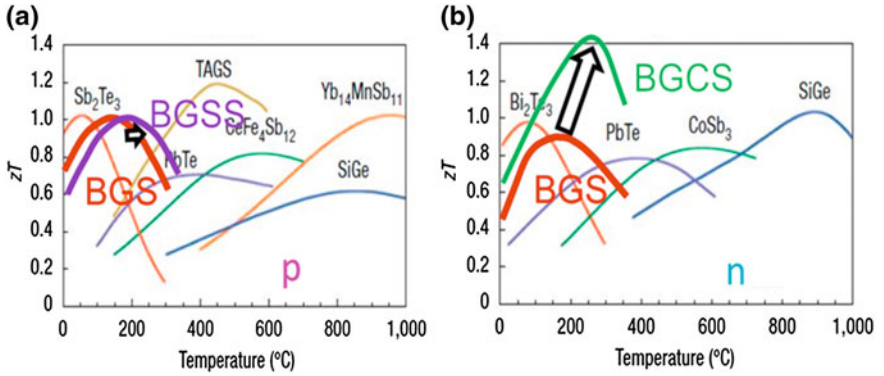

Fig. 2.18 Temperature dependence the thermoelectric dimensionless figure merit *ZT* for type-VIII $Ba_8Ga_{16}Sn_{30}$ (BGS), $Ba_8Ga_{16+x}Sn_{30-x-y}Sb_y$(BGSS), and $Ba_8Ga_{16-x}Cu_xSn_{30}$ (BGCS). Other data are represented from Ref. [11]

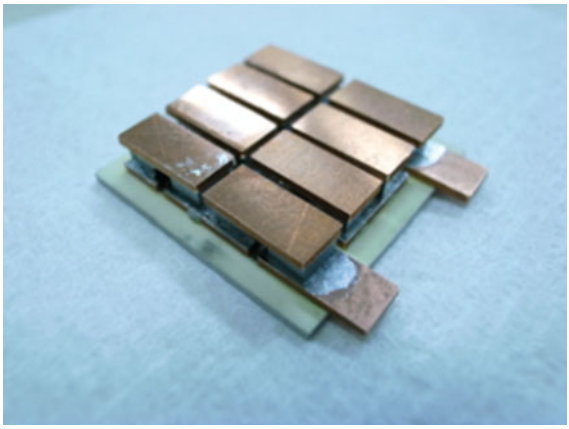

Fig. 2.19 Thermoelectric module made of 8-pair legs of *p*- and *n*-type $Ba_8Ga_{16}Sn_{30}$ single crystals. The total dimension is $28 \times 28 \times 5.4$ mm

Acknowledgments The author gratefully acknowledges D. Huo, M. A. Avila, K. Suekuni, S-K. Den, B. Du, and Y. Saiga for their fruitful collaboration in the study of thermoelectric clathrates. This work was supported by a NEDO grant no. 09002139-0 and Grant-in-Aid from Scientific Research from MEXT of Japan, grant no. 19051011 and no. 20102004.

References

1. G.A. Slack, in *CRC Handbook of Thermoelectrics*, ed. by D.M. Rowe (CRC, Boca Raton, 1995), p. 407
2. B.C. Sales, D. Mandrus, R.K. Williams, Science **272**, 1325 (1996)
3. C. Uher, in *Handbook of Thermoelectrics: Macro to Nano*, ed. by D.M. Rowe (CRC Press, Taylor & Francies Group, Bocs Raton, 2006), Chap. 34 and references therein

4. X. Shi, H. Kong, C.P. Li, C. Uher, J. Yang, J.R. Salvador, H. Wang, L. Chen, W. Zhang, Appl. Phys. Lett. **92**, 182101 (2008)
5. D. Wee, Kozinsky, An Li, N. Marzari, M. Fornari. Phys. Rev. B **81**, 045204 (2010)
6. G.S. Nolas, J.L. Cohn, G.A. Slack, S.B. Schujman, Appl. Phys. Lett. **73**, 178 (1998)
7. V.L. Kuznetsov, L.A. Kuznetsova, A.E. Kaliazin, D.M. Rowe, J. Appl. Phys. **87**, 7871 (2000)
8. P. Rogl, in *Handbook of Thermoelectrics: Macro to Nano*, ed. by D.M. Rowe (CRC Press, Taylor & Francies Group, Bocs Raton, 2006), Chap. 32 and references therein
9. G.S. Nolas, in *Handbook of Thermoelectrics: Macro to Nano*, ed. by D.M. Rowe (CRC Press, Taylor & Francies Group, Bocs Raton, 2006), Chap. 33 and references therein
10. A. Saramat, G. Svensson, A.E.C. Palmqvist, C. Stiewe, E. Mueller, D. Platzek, S.G.K. Williams, D.M. Rowe, J.D. Bryan, G.D. Stucky, J. Appl. Phys. **99**, 023708 (2006)
11. G.J. Snyder, E.S. Toberer, Nat. Mater. **7**, 105 (2008)
12. E.S. Toberer, A.F. May, G.J. Snyder, Chem. Mater. **22**, 624 (2010)
13. B.C. Sales, B.C. Chakoumakos, R. Jin, J.R. Thompson, D. Mandrus, Phys. Rev. B **63**, 245113 (2001)
14. K. Suekuni, M.A. Avila, K. Umeo, H. Fukuoka, S. Yamanaka, T. Nakagawa, T. Takabatake, Phys. Rev. B **77**, 235119 (2008)
15. M. Christensen, A.B. Abrahamsen, N.B. Christensen, F. Juranyi, N.H. Andersen, K. Lefmann, J. Andreasson, C.R.H. Bahl, B.B. Iversen, Nat. Mater. **7**, 811 (2008)
16. M. Christensen, S. Johnsen, B.B. Iversen, Dalton Trans. **39**, 978 (2010)
17. E.S. Toberer, A. Zevelkink, G.J. Snyder, J. Mater. Chem. **21**, 15843 (2011)
18. T. Nakayama, E. Kaneshita, J. Phys. Soc. Jpn. **80**, 104604 (2011)
19. A.V. Shevelkov, K. Kovnir, in *Structure and Bonding 139*, ed. by T.F. Fässler, (Springer, Berlin, 2011), p. 97
20. B. Eisenmann, H. Schäfer, R. Zagler, J. Less-Common Met. **118**, 43 (1986)
21. H.G. von Schnering, W. Carrillo-Cabrera, R. Kröner, E.-M. Peters, K. Peters, Z. Kristallogr, New Cryst. Struct. **213**, 679 (1998)
22. S. Paschen, W. Carrillo-Cabrera, A. Bentien, V.H. Tran, M. Baenitz, Y. Grin, F. Steglich, Phys. Rev. B **64**, 214404 (2001)
23. K. Kishimoto, N. Ikeda, K. Akai, T. Koyanagi, Appl. Phys. Express **1**, 031201 (2008)
24. Y. Sasaki, K. Kishimoto, T. Koyanagi, H. Asada, K. Akai, J. Appl. Phys. **105**, 073702 (2009)
25. D. Huo, T. Sakata, M.A. Avila, M. Tsubota, F. Iga, H. Fukuoka, S. Yamanaka, S. Aoyagi, T. Takabatake, Phys. Rev. B **71**, 075113 (2005)
26. G.K.H. Madsen, K. Schwarz, P. Blaha, D.J. Singh, Phys. Rev. B **67**, 125212 (2003)
27. Y. Kono, N. Ohya, T. Taguchi, M.A. Avila, K. Suekuni, T. Takabatake, S. Yamamoto, K. Akai, J. Appl. Phys. **107**, 123720 (2010)
28. M.A. Avila, K. Suekuni, K. Umeo, H. Fukuoka, S. Yamanaka, T. Takabatake, Appl. Phys. Lett. **92**, 041901 (2008)
29. Y. Saiga, K. Suekuni, B. Du, T. Takabatake, Solid State Commun. **152**, 1902 (2012)
30. B. Du, Y. Saiga, K. Kajisa, T. Takabatake, E. Nishibori, H. Sawa, Phil. Mag. **92**, 2541 (2012)
31. H.J. Goldsmid, *Introduction to Thermoelectricity* (Springer, Heidelberg, 2010)
32. Y. Saiga, K. Suekuni, S.K. Deng, T. Yamamoto, Y. Kono, N. Ohya, T. Takabatake, J. Alloys Compd. **507**, 1 (2010)
33. H.J. Goldsmid, J.W. Sharp, J. Electron. Matter **28**, 869 (1999)
34. S. Deng, Y. Saiga, K. Suekuni, T. Takabatake, J. Appl. Phys. **108**, 073705 (2010)
35. S. Deng, Y. Saiga, K. Kajisa, T. Takabatake, J. Appl. Phys. **109**, 103704 (2011)
36. Y. Saiga, B. Du, S.K. Deng, K. Kajisa, T. Takabatake, J. Alloys Compd. **537**, 303 (2012)
37. B. Du, Y. Saiga, K. Kajisa, T. Takabatake, J. Appl. Phys. **111**, 013707 (2012)
38. Y. Kono, N. Ohya, Y. Saiga, K. Suekuni, T. Takabatake, K. Akai, S. Yamamoto, J. Electric Mater. **40**, 845 (2011)

http://www.springer.com/978-3-642-37536-1

Thermoelectric Nanomaterials
Materials Design and Applications
Koumoto, K.; Mori, T. (Eds.)
2013, XIX, 387 p., Hardcover
ISBN: 978-3-642-37536-1